IEEE Open Journal of
Power Electronics

Received 9 December 2023; revised 12 January 2024; accepted 16 January 2024. Date of publication 23 January 2024;
date of current version 7 February 2024. The review of this article was arranged by Associate Editor Xiong Du.

Digital Object Identifier 10.1109/OJPEL.2024.3357128

Closed-Form Solutions for Grid-Forming Converters: A Design-Oriented Study

FANGZHOU ZHAO [1] (Member, IEEE), TIANHUA ZHU [1] (Member, IEEE), LENNART HARNEFORS [2] (Fellow, IEEE), BO FAN [3] (Member, IEEE), HENG WU [1] (Senior Member, IEEE), ZICHAO ZHOU [3] (Student Member, IEEE), YIN SUN [4] (Member, IEEE), AND XIONGFEI WANG [3] (Fellow, IEEE)

[1]AAU Energy, Aalborg University, 9220 Aalborg, Denmark
[2]ABB Corporate Research, SE-722 26 Västerås, Sweden
[3]Electrical Engineering, KTH Royal Institute of Technology, 114 28 Stockholm, Sweden
[4]Renewable Generation Technology, Shell Global Solutions International B.V., 2596 Den Haag, Netherlands

CORRESPONDING AUTHOR: XIONGFEI WANG (e-mail: xiongfei@kth.se)

ABSTRACT This paper derives closed-form solutions for grid-forming converters with power synchronization control (PSC) by subtly simplifying and factorizing the complex closed-loop models. The solutions can offer clear analytical insights into control-loop interactions, enabling guidelines for robust controller design. It is proved that 1) the proportional gains of PSC and alternating voltage control (AVC) can introduce negative resistance, which aggravates synchronous resonance (SR) of power control, 2) the integral gain of AVC is the cause of sub-synchronous resonance (SSR) in stiff-grid interconnections, albeit the proportional gain of AVC can help dampen the SSR, and 3) surprisingly, the current controller that dampens SR actually exacerbates SSR. Controller design guidelines are given based on analytical insights. The findings are verified by simulations and experimental results.

INDEX TERMS Grid-connected converter, grid-forming control, stability, sub-synchronous resonance, synchronous resonance.

I. INTRODUCTION

The growing penetration of voltage-source converter (VSC)-based resources in electrical grids necessitates grid-forming (GFM) capabilities for VSCs [1], [2]. Differing from conventional grid-following VSCs, the GFM capabilities requires VSCs to behave as a voltage source behind an impedance and autonomously provide power responses to maintain the voltage and frequency of power grids [3], [4], [5].

There have been extensive studies on stability and control of GFM-VSCs. It is shown that when GFM-VSCs are connected to a highly inductive grid, the synchronous-frequency resonance (SR) may be manifested by the power synchronization control (PSC) [6]. To dampen the SR, a virtual resistance (VR) that is based on the feedback of VSC output current is used in [6], [7]. Designing the VR can be done by evaluating the damping ratio of closed-loop poles of PSC, which yields an empirical value of VR, i.e., 0.2 p.u. [8], yet this approach overlooks the dynamics of alternating voltage control (AVC). Recent studies in [9], [10] indicate that AVC can affect the PSC dynamics, which in turn can affect the damping effect of VR on SR. However, there is lack of analytical interpretation of how AVC impacts the SR, particularly when the current control (CC) is implemented.

In addition to the SR, the sub-synchronous resonance (SSR) issues are reported when GFM-VSC is connected to a stiff grid with a high short-circuit ratio (SCR) [11], [12], [13], [14], [15], [16], where the SSR frequency is often around 10 Hz. Interactions caused by CC and AVC are respectively identified as the causes of SSR in [11] and [12], implying that the SSR phenomenon may vary with the design of inner control loops. The study in [11] presents a design-oriented analysis of SSR by investigating the poles of equivalent PSC plant in the closed-form. However, the impacts of AVC are still overlooked. By incorporating the AVC into a closed-loop model of GFM-VSC, the studies in [12], [13], [14], [15] can fully characterize the SSR behavior, yet they are based on

TABLE 1. Three Schemes of GFM Controls With Different Inner Loops (Low-Pass Filters Not Depicted)

Scheme 1	Scheme 2	Scheme 3
PSC	PSC and AVC	PSC, AVC, CC and VFF
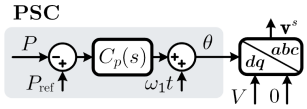	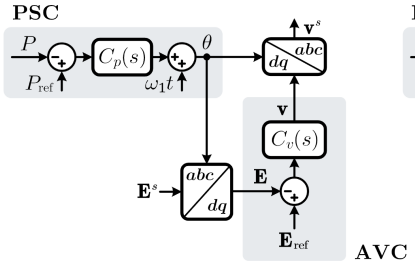	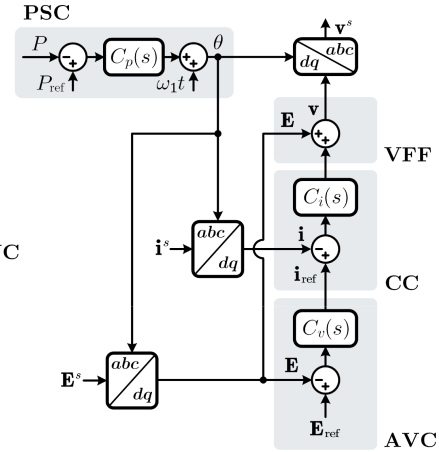

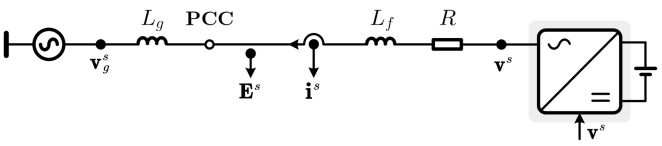

FIGURE 1. Single-line diagram of a grid-connected three-phase VSC.

numerical studies, e.g., sensitivity analysis of control and circuit parameters. Consequently, the findings are case-specific, and the design guidelines of controllers tend to be empirical, which limits their generality for different operating conditions and system configurations.

This paper thus proposes a robust, analytical design approach for GFM-VSCs that help mitigate the risks of SR and SSR. The major contribution is the generalized closed-form solutions of the GFM control, considering different combinations of PSC, AVC and CC loops. Differing from numerical analysis, the analytical solutions not only shed insights into the conditions and causes of SR and SSR, but they also provide physical interpretations on impacts of different controllers, which enables to formulate a general guideline for GFM control design and parameter-tuning.

This paper is structured as follows. Section II describes the GFM-VSC system under study and the denotations of physical variables used in this work. Section III provides the closed-form solutions of GFM-VSC with PSC only. Section IV discusses closed-form solutions of GFM-VSC with both PSC and AVC, while Section V explores the control with PSC, AVC, and CC. A summary of the stability analysis of all control schemes is presented in Section VI, followed by experimental verifications in Section VII. Conclusions are finally drawn in Section VIII.

II. SYSTEM DESCRIPTION

Fig. 1 shows a single-line diagram of the three-phase grid-connected VSC, and Table 1 presents the GFM control schemes for analysis. To reveal the impact of each control loop, which includes PSC, AVC, CC, and voltage feedforward (VFF), three schemes are considered in Table 1 to give a step-by-step study. The dc-link voltage is assumed to be constant in this study, as it can be regulated by a front-end converter or an energy storage system [11]. An L filter is used with the VSC, and it is denoted by the inductance L_f and equivalent series resistance (ESR) R. The grid is denoted by a voltage source behind an inductance L_g [8], where L_g is quantified by the SCR, seen from the point of common coupling (PCC), which is expressed as [17]

$$\mathrm{SCR} = 1/\left(\omega_1 L_g\right) \tag{1}$$

where ω_1 is the fundamental frequency, and $\omega_1 L_g$ is calculated in per-unit (p.u.) value (base value will be introduced later).

The voltages and currents are denoted in stationary reference frame by complex space vectors [18], e.g., output voltage vector $\mathbf{E}^s$ and output current vector $\mathbf{i}^s$, and their corresponding denotations in the rotating dq-frame do not have the superscript ^{s} [9], e.g., $\mathbf{i} = i_d + ji_q$. In PSC, the active power P is calculated by

$$P = \kappa \mathrm{Re}\left\{\mathbf{E}^s\left(\mathbf{i}^s\right)^*\right\} = \kappa \mathrm{Re}\left\{\mathbf{E}\mathbf{i}^*\right\}, \kappa = 3/\left(2K^2\right) \tag{2}$$

where $\mathbf{E}^s$ and $\mathbf{E}$ are the PCC voltage vectors in the stationary frame and the dq-frame, respectively, and K is the space vector scaling constant. For peak-value scaling ($K = 1$), $\kappa = 3/2$. For p.u. normalization of the quantities or power-invariant scaling ($K = \sqrt{3/2}$), $\kappa = 1$ [8]. The superscript * in (2) denotes the complex conjugate.

In this work, all controls and modeling are conducted using p.u. values ($\kappa = 1$), with the conclusions being consistent when translated into real values. The base value of all voltages is peak nominal phase voltage E_B. Likewise, the base current is peak nominal phase current I_B. Hence, the base impedance is given by $Z_B = E_B/I_B$, while base admittance is $Y_B = 1/Z_B$. With (2), the base power is defined as $P_B = 1.5E_BI_B$.

The typical PSC controller – an integrator [6] – is used in this study, and $C_p(s)$ is defined as

$$C_p(s) = k_P/(\kappa s). \tag{3}$$

where the base value of the controller gain k_P is $k_B = \kappa/P_B$. k_P is usually small, and a typical range is $0.01\omega_1 \sim 0.05\omega_1$ [1], [19].

The AVC in dq-frame often uses proportional integral (PI) controllers [20], and $C_v(s)$ is defined as

$$C_v(s) = G_a + k_i/s. \tag{4}$$

In scheme 2, the base value of G_a and k_i is 1, therefore the p.u. values and real values are the same. While in scheme 3, the base value of G_a and k_i is $Y_B = I_B/E_B$.

The CC and VFF are used to regulate fast current dynamics during faults [21]. The current limiter [22] between AVC and CC is not plotted for simplicity, as it does not affect small-signal dynamics [25]. The CC in dq-frame also employs PI controllers. However, the I gain is typically small and is commonly omitted [10], [23]. Thereby, $C_i(s)$ is defined as

$$C_i(s) = R_a \tag{5}$$

where the base value of R_a is $Z_B = E_B/I_B$.

In addition, the analysis is focused on the low-frequency (0∼100 Hz) dynamics of GFM control. The cut-off frequencies of the low-pass filters (LPFs) used within AVC and VFF are often designed to be higher than 100 Hz [10]. Hence, they are not depicted in Table 1 nor considered hereafter.

III. CLOSED-FORM SOLUTIONS FOR PSC

Scheme 1 is analyzed first, focusing only on PSC to reveal the characteristics without any inner-loop coupling. A constant voltage magnitude is used in Table 1, and $V = 1$ p.u.

The power stage model of Fig. 1 is given by

$$\mathbf{v}^s - (sL + R)\mathbf{i}^s = \mathbf{v}_g^s = V_g e^{j\omega_1 t} \tag{6}$$

where $\mathbf{v}^s$ and $\mathbf{v}_g^s$ are the converter and grid voltage vectors, respectively, and $L = L_f + L_g$ is the total inductance. Then, the corresponding dq-frame vectors in (6) and rotating angle with small-signal perturbations are defined by

$$\theta = \omega_1 t + \theta_0 + \Delta\theta,\ \mathbf{v} = \mathbf{v}_0 + \Delta\mathbf{v},\ \mathbf{i} = \mathbf{i}_0 + \Delta\mathbf{i} \tag{7}$$

where θ_0, $\mathbf{v}_0 = V$ and $\mathbf{i}_0 = i_{d0} + ji_{q0}$ denote the static values. With (7), the small-signal model of (6) is derived as [8]

$$\Delta\mathbf{v} - \left[(s + j\omega_1)L + R\right]\Delta\mathbf{i} = j\left\{\left[(s + j\omega_1)L + R\right]\mathbf{i}_0 - V\right\}\Delta\theta \tag{8}$$

where the Laplace variable s henceforth is to be considered as the operator $s = d/dt$, where appropriate. Since AVC and CC are not included, $\Delta\mathbf{v} = 0$. Thereby, (8) gives

$$\Delta\mathbf{i} = -j\frac{\left[(s + j\omega_1)L + R\right]\mathbf{i}_0 - V}{(s + j\omega_1)L + R}\Delta\theta. \tag{9}$$

By linearizing (2), the active power perturbation is given by

$$\Delta P = \kappa \mathrm{Re}\left\{\mathbf{E}_0\Delta\mathbf{i}^* + \mathbf{i}_0^*\Delta\mathbf{E}\right\}. \tag{10}$$

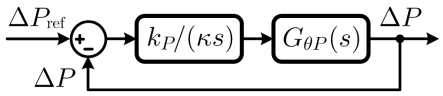

FIGURE 2. Small-signal model of PSC loop.

Similar to (8), the PCC voltage dynamics can be derived as

$$\Delta\mathbf{E} - (s + j\omega_1)L_g\Delta\mathbf{i} = j\left[(s + j\omega_1)L_g\mathbf{i}_0 - \mathbf{E}_0\right]\Delta\theta. \tag{11}$$

Substituting (9) and (11) into (10) gives the plant of PSC, i.e.,

$$\Delta P = \kappa\beta\frac{i_{q0}L_g s^2 + E_{q0}s + \omega_1\gamma}{(s + \alpha)^2 + \omega_1^2}\Delta\theta = G_{\theta P}(s)\Delta\theta \tag{12}$$

where $\alpha = R/L$, $\beta = V/L$ and $\gamma = E_{d0} + i_{q0}\omega_1 L_g$.

Based on (12), the closed-loop model of PSC is illustrated in Fig. 2, and the closed-loop transfer function is derived as

$$\Delta P = \frac{\frac{k_P}{\kappa s}G_{\theta P}(s)}{1 + \frac{k_P}{\kappa s}G_{\theta P}(s)}\Delta P_{\mathrm{ref}} = G_{\mathrm{PSC}}(s)\Delta P_{\mathrm{ref}},$$

$$G_{\mathrm{PSC}}(s) = \frac{k_P\beta\left(i_{q0}L_g s^2 + E_{q0}s + \omega_1\gamma\right)}{s^3 + (2\alpha + a_2)s^2 + \left(\omega_1^2 + \alpha^2 + a_1\right)s + k_P\beta\omega_1\gamma} \tag{13}$$

where $a_1 = k_P\beta E_{q0}$, $a_2 = k_P\beta i_{q0}L_g$, and k_P is the integral gain.

Define the following coefficients $n_1 = 2\alpha$, $n_0 = \omega_1^2$, $m_2 = a_2$, $m_1 = \alpha^2 + a_1$ and $m_0 = k_P\beta\omega_1\gamma$, and substitute them into the denominator of $G_{\mathrm{PSC}}(s)$. Then, the three poles of $G_{\mathrm{PSC}}(s)$ can be solved by setting the denominator equal to 0, i.e.,

$$s^3 + (n_1 + m_2)s^2 + (n_0 + m_1)s + m_0 = 0 \tag{14}$$

Using the rules in Appendix I, the closed-form solutions of the three poles are approximately derived as

$$\begin{aligned} G_{\mathrm{PSC}}(s) &= k_P\beta\frac{i_{q0}L_g s^2 + E_{q0}s + \omega_1\gamma}{(s - p_1)(s - p_2)(s - p_3)} \\ p_{1,2} &\approx -\frac{2R - k_P V E_{d0}/\omega_1}{2L} \\ &\quad \pm j\sqrt{\omega_1^2 - \left(\frac{2R - k_P V E_{d0}/\omega_1}{2L}\right)^2} \\ &\approx -\frac{2R - k_P V E_{d0}/\omega_1}{2L} \pm j\omega_1 \\ p_3 &\approx -k_P\left(E_{d0} + i_{q0}\omega_1 L_g\right)V/(\omega_1 L) \end{aligned} \tag{15}$$

The details are shown in Appendix I, which offers a method to simplify the cubic equation for factorization. The coefficients in this scheme can satisfy the required conditions (36) and (38) in Appendix I to obtain the approximated solutions. The model (15) is verified as follows.

Example 1: Consider a power circuit in Fig. 1 and parameters listed in Table 2. The VSC is controlled in scheme 1 in Table 1 and $k_P = 0.03\omega_1$.

TABLE 2. Parameters of Power Circuit

Symbol	Description	Value
E_n	Rated voltage (L-L, RMS)	190.5 V (1 p.u.)
P_n	Rated capacity	5 kW (1 p.u.)
ω_1	Nominal frequency	314 rad/s (50 Hz)
L_f	Filter inductance	3 mH (0.1298 p.u.)
R	ESR of filter	189 mΩ (0.026 p.u.)

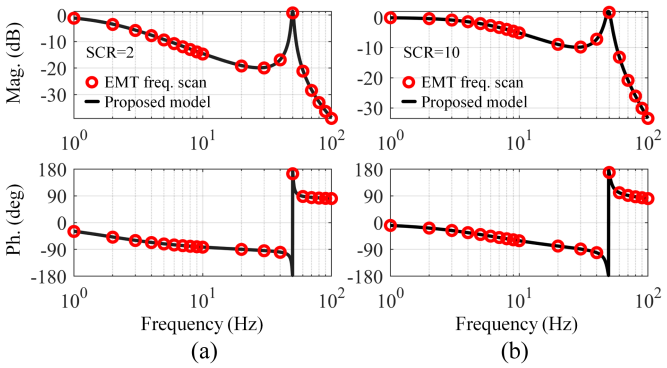

FIGURE 3. Comparison of closed-loop transfer function $G_{PSC}(s)$ in (15) and EMT simulation model. (a) SCR = 2. (b) SCR = 10.

Fig. 3 compares the frequency responses of proposed model (15) against the frequency scan results in EMT simulations for SCR = 2 and SCR = 10, respectively. The frequency scan results agree well with the model, which verifies the derivations.

In (15), the damping ratio of $p_{1,2}$ can be further derived by

$$\zeta_{1,2} \approx \frac{\omega_1 R - k_P V E_{d0}/2}{\omega_1^2 L}. \tag{16}$$

Remark 1: The following observations can be made based on (15) and (16):

1) The resistance R is important to guarantee the stability. For a VSC system with a high X/R ratio, $\zeta_{1,2}$ are small and $p_{1,2}$ tend to be under-damped. SR may present in both weak and stiff grids as long as the resistance is insufficient.
2) The PSC gain k_P negatively affects $\zeta_{1,2}$, hence a high k_P can destabilize the system. The maximum value $k_{P\max}$ that is critical to the system stability can be derived as

$$k_{P\max} = 2R\omega_1/(VE_{d0}). \tag{17}$$

Given that both $V$and E_{d0} are near 1 p.u., it can be inferred that $k_{P\max}$ is around $2R\omega_1$ in p.u. value (a typical droop selection is $0.03\omega_1$). The grid resistance, if considered, can be regarded as a part of R in (17). Thus, $k_{P\max}$ becomes higher with the increase of grid resistance. In this study, Fig. 1 only considers the ESR of L-filter, which gives the worst-case design for $k_{P\max}$.
3) In the imaginary parts of $p_{1,2}$ in (15), ω_1^2 is much larger than the other term. Thus, the oscillation frequency of $p_{1,2}$ is around the synchronous frequency ω_1, i.e., the SR mode.

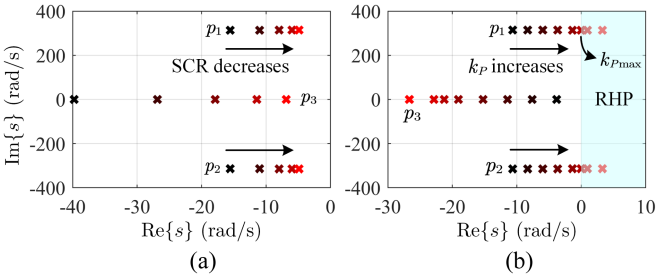

FIGURE 4. Pole-plot of $G_{PSC}(s)$. (a) SCR decreases from 10 to 1.5. (b) k_P increases from $0.01\omega_1$ to $0.07\omega_1$.

4) Provided that $k_P < k_{P\max}$, the system can remain stable under both weak- and stiff-grid conditions even if the damping is insufficient. Different grid inductance and filter $L = L_g + L_f$ in the denominator of (16) will not shift the poles to the right-half plane (RHP).

Following Example 1, Fig. 4 gives the pole-plots of $G_{PSC}(s)$. The conjugate poles $p_{1,2}$ move to the right as SCR decreases in Fig. 4(a). However, with $k_P = 0.03\omega_1 < k_{P\max} = 0.0558\omega_1$, $p_{1,2}$ will not enter the RHP, causing instability. Therefore, the system is stable irrespective of SCR. In Fig. 4(b), the increase of k_P (from $0.01\omega_1$ to $0.07\omega_1$) degrades the damping ratio. Yet, when $k_P > k_{P\max}$, $p_{1,2}$ enter the RHP, the system is unstable.

IV. CLOSED-FORM SOLUTIONS FOR PSC AND AVC

This section presents closed-form solutions for GFM control with PSC and AVC (scheme 2 in Table 1). The AVC uses a PI controller, i.e., $C_v(s) = G_a + k_i/s$. As will be proved as follows, the P gain G_a shows negative damping on SR, which is the main risk of instability. The I gain k_i is selected from [24], giving $k_i \leqslant \omega_c/10$, where ω_c is the crossover frequency. To compare with scheme 3, where the bandwidth of AVC is lower than inner loop CC (e.g., $10\omega_1$ rad/s [25]), it is assumed that $\omega_c \leqslant 10\omega_1$. Thus, k_i is set lower than ω_1, and it shows limited effect on SR compared to G_a. Consequently, k_i is omitted in this section for simplicity, but we will analyze its influence in the next section and experimental results.

Then, the dynamics of control voltage with AVC is given by

$$\Delta \mathbf{v} = -G_a \Delta \mathbf{E}. \tag{18}$$

Equation (18) is different from scheme 1 where the open-loop voltage control is used ($\Delta \mathbf{v} = 0$), but the rest of the modeling process to obtain the closed-form solutions is similar. For clarity, the complete derivations are given in Appendix II, and the results are presented as follows. It is found that the AVC can equivalently reshape the plant in Fig. 2, and therefore modifies the closed-loop transfer function of PSC $G_{PSCa}(s)$ as

$$G_{PSCa}(s) = \frac{N_a(s)}{(s-p_{1a})(s-p_{2a})(s-p_{3a})} \tag{19}$$

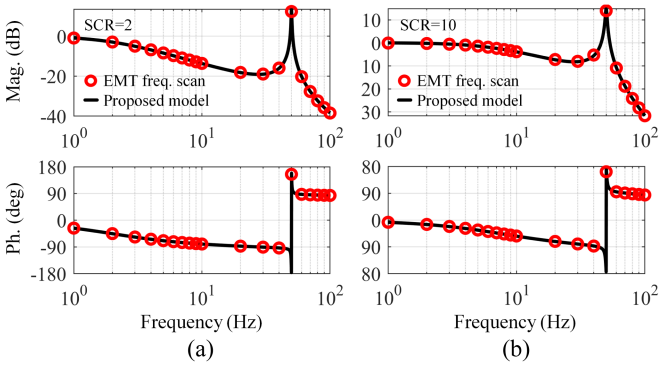

FIGURE 5. Comparison of closed-loop transfer function $G_{\text{PSCa}}(s)$ in (19) with poles (20) and EMT simulation model. (a) SCR = 2. (b) SCR = 10.

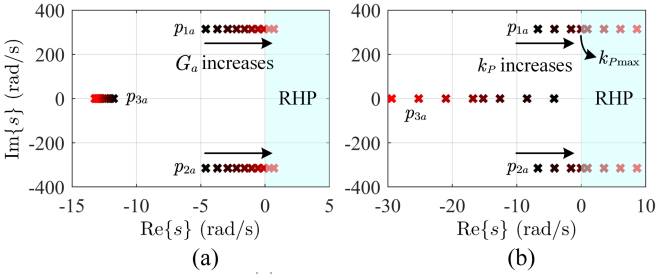

FIGURE 6. Pole-plot of $G_{\text{PSCa}}(s)$. (a) G_a increases from 0.1 to 1.0 p.u. (b) κ_P increases from $0.01\omega_1$ to $0.07\omega_1$.

where $N_a(s)$ is the nominator (detailed expression is given in Appendix II), and it also has three poles (p_{1a}, p_{2a} and p_{3a}). From Appendix II, the closed-form solutions of these poles can be approximated to

$$p_{1,2a} \approx -\frac{R-\delta}{L+G_aL_g} \pm j\omega_1,\ \delta = \frac{k_P\left(VE_{d0}+G_a|\mathbf{E}_0|^2\right)}{2\omega_1}$$
$$p_{3a} = -\frac{2\delta + k_PL_g\left(Vi_{q0}+G_a\text{Im}\left\{\mathbf{E}_0^*\mathbf{i}_0\right\}\right)}{L+G_aL_g} \tag{20}$$

The model is verified by the following example.

Example 2: Consider a power circuit in Fig. 1 and parameters listed in Table 2. The VSC is controlled in scheme 2 in Table 1. The control parameters are $k_P = 0.03\omega_1$ and $C_v(s) = G_a = 0.5$ p.u. Fig. 5 compares the model $G_{\text{PSCa}}(s)$ with poles calculated in (20) and the frequency scan results in EMT simulations when SCR = 2 and SCR = 10, respectively. The proposed model (20) agrees well with the simulation results.

Based on (20), the damping ratio of $p_{1,2a}$ can be given by

$$\zeta_{1,2a} \approx \frac{R-\delta}{\omega_1\left(L+G_aL_g\right)} \tag{21}$$

where $\delta = k_P(VE_{d0}+G_a|\mathbf{E}_0|^2)/(2\omega_1)$ is given in (20).

Remark 2: The following observations can be made based on (20) and (21):

1) The P gain G_a of AVC has two effects on $\zeta_{1,2a}$. First, G_a contributes to more negative resistance δ in the numerator, similar to PSC gain k_P. Second, it adds a virtual inductance in the denominator. Both effects decrease the damping ratio, and the risk of SR evidently increases compared to (16), where AVC is not used.
2) Due to the negative effects of AVC, the maximum control gain of PSC k_P is decreased. To guarantee the stability, i.e., $R-\delta > 0$, $k_{P\max}$ is obtained by

$$k_{P\max} = 2R\omega_1/\left(VE_{d0}+G_a|\mathbf{E}_0|^2\right). \tag{22}$$

By assuming $VE_{d0} \approx |\mathbf{E}_0|^2 \approx 1$ p.u., an estimation of $k_{P\max}$ is $k_{P\max} = 2R\omega_1/(1+G_a)$. As a result, the P controllers of AVC aggravate SR, and thus tend to destabilize the system.

Following Example 2, Fig. 6 shows the pole-plots of the model $G_{\text{PSCa}}(s)$ when G_a and k_P increase, respectively, where $p_{1,2a}$ move to the right and finally enter RHP in both cases. Fig. 8(a) shows that G_a has negative damping on SR. In Fig. 6(b), $k_{P_{\max}} = 0.0362\omega_1$ is lower than that of Example 1, where AVC is not used in Fig. 4(b)($k_{P_{\max}} = 0.0558\omega_1$).

V. CLOSED-FORM SOLUTIONS FOR PSC, AVC, CC AND VFF

This section presents closed-form solutions of GFM control, including PSC, AVC, CC and VFF (scheme 3 in Table 1). To highlight the effects of inner loop controllers on different resonances, we will discuss the AVC with P controllers first, and then come to the PI controllers for a step-by-step analysis.

A. AVC WITH P CONTROLLER

In this scheme, the P gains of AVC and CC are set as G_a and R_a, respectively. The bandwidth of CC loop typically ranges from hundred Hz to a few kHz, which results in a high P gain R_a (around 1 p.u., which is much higher than R). For instance, when $L_f = 0.1$ p.u., R_a is set to 1 p.u. to achieve a bandwidth of 500 Hz for CC [25].

Then, the dynamics of control voltage $\Delta\mathbf{v}$ with AVC, CC and VFF are expressed as

$$\Delta\mathbf{v} = R_a\left(\Delta\mathbf{i}_{\text{ref}} - \Delta\mathbf{i}\right) + \Delta\mathbf{E} = \left(-R_aG_a + 1\right)\Delta\mathbf{E} - R_a\Delta\mathbf{i}. \tag{23}$$

Appendix III gives the rest of the modeling process, which is similar to the previous Sections. The final closed-loop transfer function $G_{\text{PSCb}}(s)$ that incorporates the dynamics of AVC, CC and VFF can be obtained as

$$G_{\text{PSCb}}(s) = \frac{N_b(s)}{(s-p_{1b})(s-p_{2b})(s-p_{3b})} \tag{24}$$

where $N_b(s)$ is the nominator (detailed expression is given in Appendix III), and it also has three poles (p_{1b}, p_{2b} and p_{3b}). From Appendix III, the closed-form solutions of the conjugate poles can be approximated to

$$p_{1,2b} \approx -\frac{R+R_a}{L+\left(R_aG_a-1\right)L_g} \pm j\omega_1 \tag{25}$$

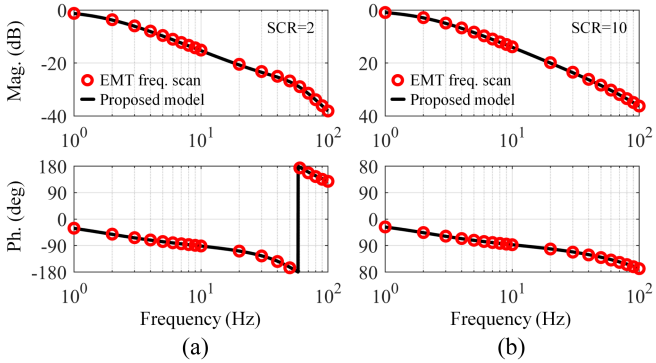

FIGURE 7. Comparison of closed-loop transfer function $G_{\text{PSCa}}(s)$ in (24) with poles (25) and EMT simulation model. (a) SCR = 2. (b) SCR = 10.

The solution of real pole p_{3b} is given in (50). The damping ratio of $p_{1,2b}$ is calculated as

$$\zeta_{1,2b} \approx \frac{R_a}{\sqrt{\omega_1^2\left[L + (R_a G_a - 1)\, L_g\right]^2 + R_a^2}} \tag{26}$$

The model is verified by the following example.

Example 4: Consider a power circuit in Fig. 1 and parameters in Table 2. The VSC uses scheme 3 in Table 1, and the control parameters are $k_P = 0.03\omega_1$, $R_a = 0.865$ p.u. and $G_a = 3$ p.u.

Fig. 7 compares the proposed model, i.e., $G_{\text{PSC}b}(s)$ with derived poles $p_{1,2b}$ in (25), and the frequency scan results in EMT simulations when SCR = 2 and SCR = 10, respectively. The frequency scans can validate the closed-form solutions.

Remark 3: The following observations can be made based on (25):

1) The CC adds a virtual resistance R_a to the real part of $p_{1,2b}$, which effectively dampens SR.
2) The AVC gain G_a equivalently adds a virtual inductance to the real parts of $p_{1,2b}$, and decreases the damping ratio for SR. However, the VFF, which yields the term "−1" in the denominator of (25), has an opposite effect.
3) With the decrease of SCR, the damping ratio $\zeta_{1,2b}$ of $p_{1,2b}$ decreases, and the worst case is $L_g = 1$ p.u. To guarantee that $\zeta_{1,2b}$ is higher than 0.707, R_a and G_a can be designed based on (25) following

$$(1 - G_a/\text{SCR})\, R_a \geqslant \omega_1 L_f \tag{27}$$

where (27) is in p.u. values and SCR is given in (1).

1) With a proper design of R_a and G_a in 3), the control shows robust stability irrespective of SCR, especially the stiff grid, where the resonance of $p_{1,2b}$ is fully damped.

Following Example 4, Fig. 8 shows the poles of $G_{\text{PSC}b}(s)$. In (a), $G_a = 3$ p.u. and R_a increases from 0.1 to 1.0 p.u. The CC can offer evident damping to $p_{1,2b}$ and mitigate the risk of SR. This allows a higher AVC gain G_a as shown in (b), compared to the case without CC in Fig. 6(a), where the system becomes unstable when G_a increases to 1 p.u.

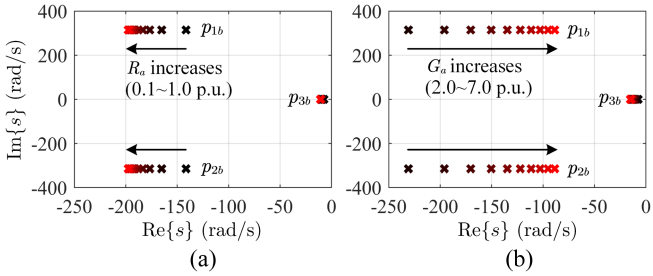

FIGURE 8. Pole-plots of $G_{\text{PSCa}}(s)$. (a) CC gain R_a increases from 0.1 to 1.0 p.u. (b) AVC gain G_a increases from 2.0 to 7.0 p.u.

B. AVC WITH PI CONTROLLER

To minimize the steady-state error of PCC voltage magnitude, the AVC needs PI controllers $C_v(s) = G_a + k_i/s$. The I gain k_i is often set lower than ω_1 in p.u. value, as explained in Section IV, and it shows limited effects on SR. Therefore, when CC (R_a) is used, the SR can be effectively damped.

However, as will be proved in the following analysis, the AVC I controllers can lead to a new risk of SSR. In this scheme, it is more difficult to solve the full-order model for any given operating conditions.

Therefore, to identify the SSR risk by closed-form solutions, we focus more on the light-load operating conditions where $\mathbf{i}_0 \approx 0$, and the key influencing factors of SSR will be identified theoretically – this is the main contribution of this subsection. For other load conditions, the SSR risk may still persist, but the closed-form solutions are too complicated to shed any insights, which deserves more studies in future.

In this case, the dynamics of $\Delta\mathbf{v}$ with AVC, CC and VFF are given as

$$\begin{aligned}\Delta\mathbf{v} &= R_a\left(\Delta\mathbf{i}_{\text{ref}} - \Delta\mathbf{i}\right) + \Delta\mathbf{E} \\ &= \left[-R_a\left(G_a + k_i/s\right) + 1\right]\Delta\mathbf{E} - R_a\Delta\mathbf{i}.\end{aligned} \tag{28}$$

Appendix IV gives the detailed models of converter under light load conditions ($\mathbf{i}_0 \approx 0$). Additionally, since SR is well-damped by CC, we only focus on the SSR by omitting the SR mode. As a result, the closed-loop transfer function $G_{\text{PSC}c}(s)$ that incorporates the dynamics of AVC, CC and VFF can be obtained in Appendix IV as follows

$$G_{\text{PSC}c}(s) \approx \frac{N_c(s)}{(s - p_{1c})(s - p_{2c})(s - p_{3c})} \tag{29}$$

where $N_c(s)$ is the nominator (detailed expression is given in Appendix IV), and it has three poles (p_{1c}, p_{2c} and p_{3c}) since the SR mode is simplified. Then, the closed-form solutions of p_{1c}, p_{2c} and p_{3c} can be approximated to

$$\begin{aligned}p_{1,2c} = {} & (\rho_1 - \rho_2)\frac{R_a k_i L_g}{2L_{eqc}} - \frac{k_P G_a \psi}{2} \\ & \pm j\sqrt{\frac{k_i k_P \psi}{\rho_1} - \left[(\rho_1 - \rho_2)\frac{R_a k_i L_g}{2L_{eqc}} - \frac{k_P G_a \psi}{2}\right]^2}\end{aligned}$$

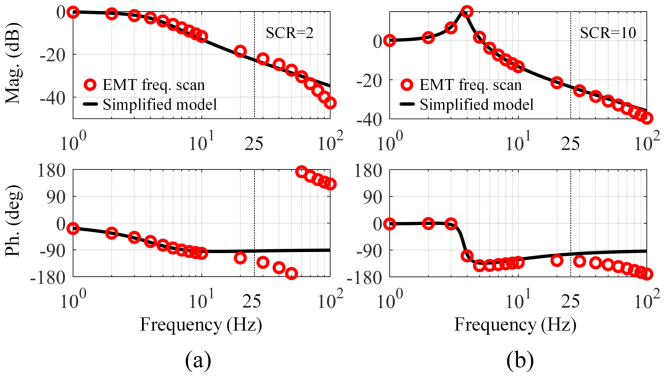

FIGURE 9. Comparison of simplified closed-loop transfer function model in (29) with poles (30) and EMT simulation model (allowable accuracy within a frequency range of 0 Hz ~ 25 Hz). (a) SCR = 2. (b) SCR = 10.

$$p_{3c} = -\frac{R_a k_i L_g}{L_f + 2R_a L_g G_a} \tag{30}$$

where

$$L_{eqc} = L_f + R_a G_a L_g,\ \psi = \frac{V^2 R_a/\omega_1 L_{eqc}}{\left[\frac{R_a(1+k_i L_g)}{\omega_1 L_{eqc}}\right]^2 + 1},$$
$$\rho_1 = \frac{L_f + R_a L_g G_a}{L_f + 2R_a L_g G_a},\ \rho_2 = \frac{2}{\left[\frac{R_a(1+k_i L_g)}{\omega_1 L_{eqc}}\right]^2 + 1}, \tag{31}$$

The model is verified by the following example.

Example 5: Consider a power circuit in Fig. 1 and parameters listed in Table 2. The VSC is controlled in scheme 3 in Table 1 The control parameters are $k_P = 0.03\omega_1$, $R_a = 0.865$ p.u., $G_a = 3$ p.u. and $k_i = 100$ p.u.

Fig. 9 compares the proposed model, i.e., (29) and (30), and EMT simulation results when SCR = 2 and SCR = 10, respectively. The proposed model with proper simplifications shows good accuracy within the frequency range below 25 Hz. Therefore, it is sufficient to characterize the SSR issues such as the resonance peak under strong grids conditions in Fig. 9(b).

Remark 4: The following observations can be made based on (30) and (31):

1) When the grid is stiff, the oscillation frequency of $p_{1,2c}$ (imaginary part) satisfies

$$\mathrm{Im}\{p_{1,2c}\} = \sqrt{\frac{k_i k_P \psi}{\rho_1} - \left[(\rho_1 - \rho_2)\frac{R_a k_i L_g}{2L_{eqc}} - \frac{k_P G_a \psi}{2}\right]^2}$$
$$< \sqrt{\frac{k_i k_P \psi}{\rho_1}} < \sqrt{0.25 k_i \omega_1 V^2}. \tag{32}$$

See Appendix V for complete derivations. To obtain (32), the parameters are assumed to be reasonably designed, e.g., a low droop value $k_P \leqslant 0.05\omega_1$ [1] and a proper CC gain $R_a \approx 1$ p.u. to give a fast CC bandwidth around 500 Hz [23].

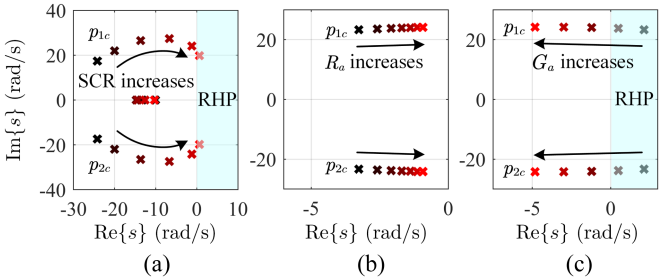

FIGURE 10. Plots of poles $p_{1,2c}$. (a) SCR increases from 1.5 to 20. (b) R_a increases from 0.4 to 1.0 p.u. (c) G_a increases from 2 to 4 p.u.

In practice, a low value of k_i is often used. If we assume $k_i < \omega_1$ and $V \approx 1$ p.u., the oscillation frequency satisfies

$$\omega_{1,2c} < 0.5\omega_1 \tag{33}$$

(33) indicates the resonance is SSR (<25 Hz).

2) Since ρ_1, ρ_2 and $\psi > 0$, the system will be unstable ($p_{1,2c}$ move to RHP) only when $\rho_1 - \rho_2 > 0$.
As the grid impedance L_g decreases, ρ_1 tends to be 1, while ρ_2 decreases and is much closer to 0. This gives a high risk of instability (positive real parts of $p_{1,2c}$). The stiff-grid conditions can cause SSR introduced by $p_{1,2c}$, while the risk of SSR is much lower under weak grid conditions.
Additionally, increasing CC gain R_a can further reduce ρ_2 that may cause SSR. This behavior is opposite to the damping of SR, as proved in Section V-A.
3) Increasing AVC P gain G_a is helpful to move $p_{1,2c}$ to the left and thus mitigate the SSR, as indicated by the real part in (30). This behavior is also opposite to the damping of SR, as proved in Section V-A.
4) The system is always stable when $\rho_1 - \rho_2 \leqslant 0$. Considering that $\rho_1 < 1$, one can find a sufficient condition to estimate stability, i.e., $\rho_2 > 1$. Then substituting (31) into $\rho_2 > 1$, an interesting conclusion is given as follows – by selecting the parameters $G_a - k_i/\omega_1 > 0$, the system is guaranteed to be stable when SCR meets

$$\mathrm{SCR} < \frac{G_a - k_i/\omega_1}{1 - \omega_1 L_f/R_a}. \tag{34}$$

See Appendix VI for proof. Equation (34) is in p.u. value, and it is a sufficient condition to give a conservative design of the parameters. Equation (34) also indicates lower values for k_i and R_a, and a higher value of G_a to guarantee the stability for stiff grid interconnections.

Following Example 5, Fig. 10 shows the poles of $G_{\mathrm{PSCc}}(s)$with respect to SCR, R_a and G_a, respectively. When SCR increases, $p_{1,2c}$ move to the right and finally enter RHP in Fig. 10(a), indicating instability of stiff-grid connections. Increasing CC gain R_a degrades the damping ratio in Fig. 10(b). However, a higher AVC P gain G_a can shift the

TABLE 3. Summary of Instability Risks and Design Guidelines of GFM Controls With Respect To 3 Schemes

Scheme (different controls)	Instability risk (SR or SSR), condition and cause	Design guidelines for controller parameters
Scheme 1 PSC (k_P/s)	**SR (50 Hz).** Condition – system with a high X/R ratio. Cause – Insufficient resistance in PSC plant and virtual negative resistance caused by k_P.	Select $k_P < k_{P\max} = 2R\omega_1/(VE_{d0})$ in (17). Damping to SR can be enhanced by decreasing k_P.
Scheme 2 PSC (k_P/s) and AVC ($G_a + k_i/s$)	**SR (worse than scheme 1).** Condition – system with high X/R ratio. Cause –Insufficient resistance in PSC plant and virtual negative resistance caused by both k_P and G_a.	Select k_P and G_a to meet $k_P < k_{P\max} = 2\omega_1 R/\left(VE_{d0} + G_a|\mathbf{E}_0|^2\right)$ in (22). Damping to SR can be enhanced by decreasing k_P or G_a.
Scheme 3 PSC (k_P/s), AVC ($G_a + k_i/s$) and CC (R_a)	**SSR (CC can effectively dampen SR).** Condition – strong grids. Cause – interactions between PSC and AVC integrators, which introduce new poles and resonance (< 25 Hz).	Select G_a, k_i and R_a to meet (34) to ensure stability (a conservative design). Damping to SSR can be enhanced by increasing G_a, or decreasing R_a or k_i.

poles to the left, as shown in Fig. 10(c), which effectively enhances the damping ratio. The effects of R_a and G_a on SSR in Fig. 10(b) and (c) are exactly opposite to Fig. 8(a) and (b) on SR. These characteristics agree well with the insights above.

VI. SUMMARY AND DESIGN GUIDANCE

Table 3 presents a summary of the instability risks of GFM controls with respect to the 3 schemes analyzed above. There are two instability risks – the SR (oscillation frequency around 50 Hz) and the SSR (oscillation frequency lower than 25 Hz).

On the one hand, the occurrence of SR is often attributed to an insufficient level of system resistance (a high *X*/*R* ratio), which limits the PSC gain k_P in scheme 1. The SR may appear under weak and stiff grid conditions. The PSC gain operates as negative resistance, reducing the damping effect to SR. The P controllers (G_a) of AVC in scheme 2 also denote to negative resistance, further decreasing the damping to SR and leads to a higher risk of instability. In scheme 3, the P controllers (R_a) of CC act as equivalent resistance, which can effectively dampen SR. Hence, under the condition that R_a is adequate, scheme 3 is devoid of the SR risk.

On the other hand, scheme 3 shows the SSR risk under light-load conditions, which is caused by the interactions between PSC and AVC integrators in stiff-grid connections. In this case, increasing G_a or decreasing R_a can enhance the damping ratio to SSR and mitigate the resonance. However, it is suggested to consider both SR and SSR when choosing these parameters since they have opposing effects. For instance, an excessive value of R_a to dampen SR may, in turn, exacerbates SSR. In addition, the risk of SSR in weak grid conditions is significantly lower compared to stiff grids.

The design guidelines for key controller parameters are also summarized in Table 3 based on the closed-form models. Note that the conditions (17) and (22) for scheme 1 and 2 are both necessary and sufficient, thus the parameters k_P and G_a can be simply selected. In contrast, scheme 3 presents additional trade-offs and more parameters, with condition (34) being only sufficient. This poses greater challenges in parameter design. Hence, based on the analysis in Section V, we suggest the following design flow for scheme 3 under the given SCR condition:

1) Select R_a based on the requirement of CC bandwidth [23]. A common requirement is to keep the bandwidth below 0.2 of the switching frequency [29], while maximizing it for fast current limitation during faults [22]. This often leads to a high value of R_a around or even exceeding 1 p.u. [25].
2) With R_a selected in 1), G_a can be designed following (27). This ensures a sufficient damping ratio for SR mode higher than 0.707. Meanwhile, choose G_a to be as high as possible while satisfying (27), fully leveraging the positive damping effect of G_a on SSR. Note that the AVC bandwidth should be lower than CC, and this can be easily ensured by using LPFs in series with G_a [10].
3) Finally, select k_i based on (34) to mitigate the risk of SSR. If (34) cannot be satisfied for very high SCR conditions, it is recommended to further raise G_a for enhanced damping to SSR. However, this may violate the design (27) in step 2). This represents a trade-off between the damping to SR and SSR. While reducing R_a is helpful, it is not suggested, as a fast CC bandwidth is crucial for fault protection.

This design flow provides explicit parameter guidelines for scheme 3 under specific SCR conditions. However, as noted earlier, scheme 3 may present stability limitations when SCR varies widely, especially for stiff grids with high SCRs. These limitations cannot be addressed solely through parameter tuning without trade-offs. To overcome the challenges associated with stiff-grid connections, more advanced control methods can be employed, e.g., [10], [26], [27].

VII. EXPERIMENTAL VERIFICATION

Fig. 11 shows the diagram of experimental setup, and the parameters are listed in Table 4. The controller is dSPACE DS1007. An *LC*-filter is employed ($C = 10\ \mu$F), and the dc-link voltage is maintained by an independent dc source. The 3 control schemes in Table 1 are evaluated respectively under both stiff and weak grid conditions.

A. STIFF GRID (SCR≈10)

Fig. 12 presents a detailed comparison of active power step responses (P_{ref}, P, output voltage E_a and current i_a of phase a) for the aforementioned controls when SCR≈10 ($L_g = 4$ mH).

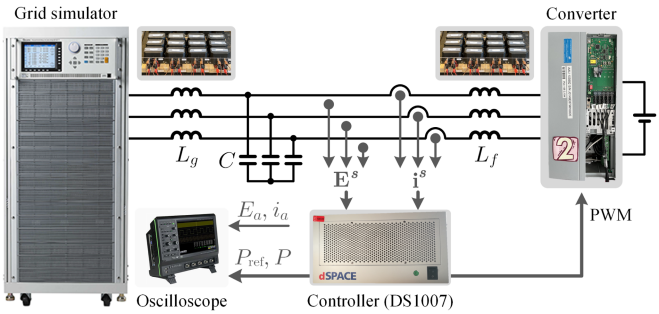

FIGURE 11. Diagram of experimental setup.

TABLE 4. Parameters of Experimental Setup

Symbol	Description	Value
E_n	Rated voltage (L-L, RMS)	190.5 V (1 p.u.)
P_n	Rated capacity	3 kW (1 p.u.)
ω_1	Nominal frequency	314 rad/s (50 Hz)
Z_{Base}	Base impedance	12.1 Ω
L_f	Filter inductance	3 mH (0.078 p.u.)
C	Filter capacitance	10 μF (0.038 p.u.)
E_{dc}	DC-link voltage	600 V (1 p.u.)
f_s	Switching frequency	10 kHz

1) SCHEME 1

In Fig. 12(a), the PSC in scheme 1 reveals clear active power oscillation around 50 Hz (≈20 ms) when $k_P = 0.06\omega_1$. The SR can be tracked back to the under-damped conjugate poles $p_{1,2}$ identified in Section III. Note that the SR on power indicates a resonance close to 0 Hz in current due to frequency coupling issue [28]. This is proved by the presence of a dc-offset in phase a current in Fig. 12(a).

Fig. 12(b) compares the step responses of PSC when k_P is decreased to $0.03\omega_1$. Clearly, the SR is mitigated. This agrees well with the conclusion in Section III that the PSC gain k_P has a negative damping effect on SR.

2) SCHEME 2

The performance of PSC ($k_P = 0.06\omega_1$) and AVC using P controllers ($G_a = 0.25$ p.u.) is shown in Fig. 12(c). Despite the use of a low value of G_a, the damping to SR decreases evidently. It takes a longer time to enter steady-state and results in a higher dc-offset in phase a current when compared to PSC in Fig. 12(a). Similar to PSC gain k_P, the P controller gain (G_a) of AVC also has a negative damping effect on SR. The explanation for this phenomenon can be found in Section IV.

In Fig. 12(d), we further evaluate the PSC ($k_P = 0.06\omega_1$) and AVC using integrators (k_i/s, $k_i = 30$ p.u.). It also presents clear power oscillations around 50 Hz. By comparing (a) and (d), it is evident that the SR issues are similar.

3) SCHEME 3

Fig. 12(e) shows the responses of scheme 3 when AVC only uses P controllers. In this case, $k_P = 0.06\omega_1$, $G_a = 0.25$ p.u., and a low value of $R_a = 0.2$ p.u. is chosen to avoid a significant static error of AVC due to the absence of AVC integrators. Upon comparing (a), (c) and (e), it is found that the SR is effectively suppressed by the CC. This provides further evidence to support the effectiveness of the CC in offering equivalent resistance and critical damping to SR, as proved in Section V-A. Note that this case is mainly used to demonstrate the effects of CC, whereas in practice, AVC often employs PI controllers to maintain a voltage magnitude of 1 p.u. without steady-state error.

Fig. 12(f) shows the response of scheme 3 when AVC uses PI controllers. The bandwidth of CC is set to 375 Hz, giving $R_a = 0.6$ p.u. according to [23]. The parameters of AVC PI controllers are $G_a = 0.25$ p.u. and $k_i = 30$ p.u. The SR is well-dampened by CC, however, an even more serious SSR around 10 Hz (100 ms) is observed. This finding is consistent with the conclusions in Section V-B – the new resonance is introduced by $p_{1,2c}$ under stiff-grid conditions, which occurs below 25 Hz and originates from the I controllers of AVC. The emergence of $p_{1,2c}$ poses a potential risk of SSR, especially when SCR varies over a wide range. The CC can enhance the damping to SR, but not SSR.

Moreover, to validate the guidelines on parameter tuning of scheme 3, Fig. 13 presents a comparison of their active power responses. In Fig. 13(a), $k_P = 0.06\omega_1$, $G_a = 0.25$ p.u., $k_i = 30$ p.u. and R_a is decreased from 0.6 to 0.3 p.u. It helps to mitigate the low-frequency oscillation compared to Fig. 12(f). A low CC bandwidth is desirable from this point. However, it is a common practice to limit the overcurrent in a fault event by employing a fast CC, which often results in a high gain of R_a. This trade-off should be considered. Another method to dampen SSR is to decrease k_i, as shown in Fig. 13(b), where $k_P = 0.06\omega_1$, $G_a = 0.25$ p.u., $k_i = 10$ p.u. and $R_a = 0.6$ p.u. Compared to Fig. 12(f), when k_i is decreased, the SSR in Fig. 13(b) evidently reduces. Finally, in Fig. 13(c), G_a is increased from 0.25 p.u. to 0.75 p.u., while $k_P = 0.06\omega_1$, $k_i = 30$ p.u. and $R_a = 0.6$ p.u. The damping ratio to SSR is effectively improved as shown in Fig. 13(c). Therefore, it is beneficial to select a higher AVC P gain (G_a) but keep a relatively low value of I gain (k_i) for SSR mitigation. These results can corroborate the remarks in Section V-B.

B. WEAK GRID (SCR≈2)

Fig. 14 shows the comparison of active power responses of all schemes in Table 1 when SCR≈2 ($L_g = 19$ mH). The X/R ratio of line impedance is approximately 7, and this weak grid offers much more resistance to SR than the stiff grid does (more than 4 times that of the stiff-grid case). As a result, PSC (scheme 1) in Fig. 14(a) with $k_P = 0.06\omega_1$ demonstrates no oscillation near fundamental frequency, unlike in Fig. 12(a) in stiff grid. The grid resistance can mitigate the negative damping caused by k_P in PSC, as indicated by (16). Fig. 14(b) shows the results of scheme 2 when $k_P = 0.06\omega_1$, $G_a = 0.25$ p.u. and $k_i = 30$ p.u. Due to the grid resistance, there is no SR issue either, compared to Fig. 12(c) and (d). Further, Fig. 14(c) shows the response of scheme 3 when $k_P = 0.06\omega_1$, $G_a = 0.25$ p.u., $k_i = 30$ p.u. and $R_a = 0.6$ p.u. It

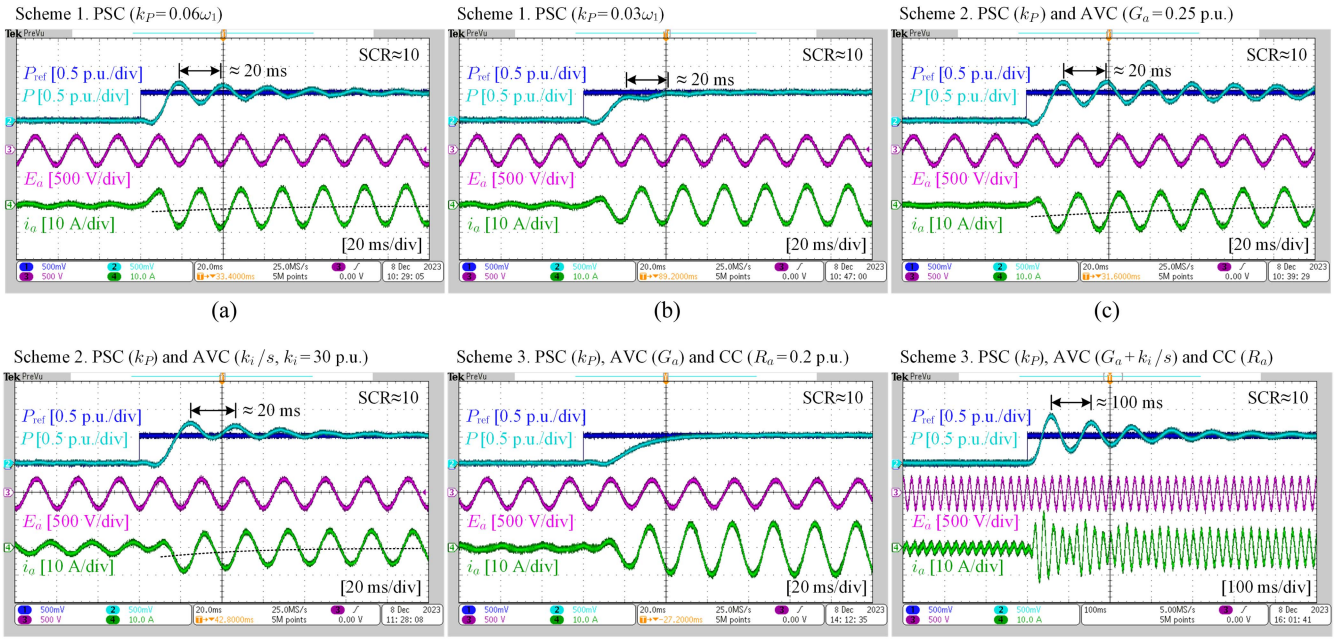

FIGURE 12. Comparison of active power responses of 3 control schemes in Table 1 when SCR≈10. (a) Scheme 1 ($k_P = 0.06\omega_1$ p.u.). (b) Scheme 1 ($k_P = 0.03\omega_1$). (c) Scheme 2 (PSC $k_P = 0.06\omega_1$, AVC using P controllers $G_a = 0.25$ p.u.). (d) Scheme 2 (PSC $k_P = 0.06\omega_1$, AVC using I controllers $k_i = 30$ p.u.). (e) Scheme 3 (PSC $k_P = 0.06\omega_1$, AVC using P controllers $G_a = 0.25$ p.u., CC $R_a = 0.2$ p.u.). (f) Scheme 3 (PSC $k_P = 0.06\omega_1$, AVC using PI controllers $G_a = 0.25$ p.u., $k_i = 30$ p.u., CC $R_a = 0.6$ p.u.).

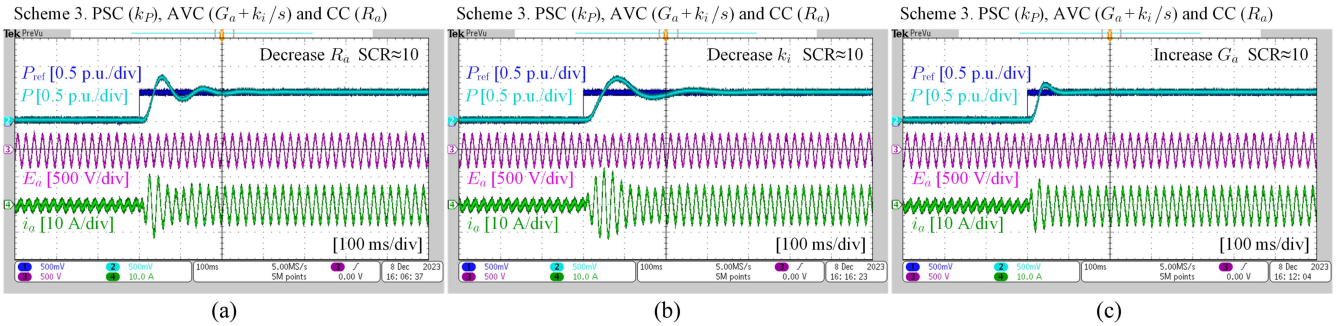

FIGURE 13. Comparison of active power responses of scheme 3 in Table 1 with different control parameters when SCR≈10. (a) Decreasing R_a to 0.3 p.u. (PSC $k_P = 0.06\omega_1$, AVC using PI controllers $G_a = 0.25$ p.u., $k_i = 30$ p.u., CC $R_a = 0.3$ p.u.). (b) Decreasing k_i to 10 p.u. (PSC $k_P = 0.06\omega_1$, AVC using PI controllers $G_a = 0.25$ p.u., $k_i = 10$ p.u., CC $R_a = 0.6$ p.u.). (c) Increasing G_a to 0.75 p.u. (PSC $k_P = 0.06\omega_1$, AVC using PI controllers $G_a = 0.75$ p.u., $k_i = 30$ p.u., CC $R_a = 0.6$ p.u.).

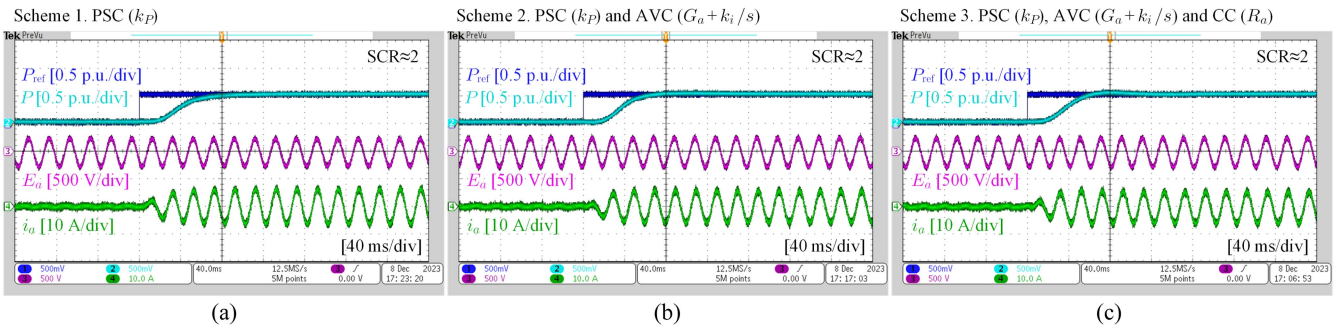

FIGURE 14. Comparison of active power responses of 3 schemes in Table 1 when SCR≈2. (a) Scheme 1 ($k_P = 0.06\omega_1$). (b) Scheme 2 (PSC $k_P = 0.06\omega_1$, AVC using PI controllers $G_a = 0.25$ p.u., $\kappa_i = 30$ p.u.). (c) Scheme 3 (PSC $k_P = 0.06\omega_1$, AVC using PI controllers $G_a = 0.25$ p.u., $\kappa_i = 30$ p.u., CC $R_a = 0.6$ p.u.).

demonstrates that the risk of SSR is much lower under weak grids conditions than stiff grids as shown in Fig. 12(f), which can verify the analysis of SSR in Section V-B. The conjugate poles have adequate damping in all three cases when the SCR is low, and hence, the real pole determines the power dynamic performances. Consequently, when the power system presents sufficient grid resistance (e.g., *X*/*R* ratio no greater than 10), the stiff-grid interconnection of GFM converter is more prone to resonances (SR or SSR) than weak ones.

VIII. CONCLUSION

This paper fully investigates the dynamics of PSC coupled with AVC and CC by deriving closed-form solutions of poles to gain insights into designing stable GFM controls. To sum up, the primary results can be outlined as follows.

1) Resistance insufficiency is the cause of SR. The PSC gain and AVC P controller gain introduce negative resistance to SR, which degrades the damping.
2) CC can provide critical equivalent resistance to counteract the effects above and dampen SR.
3) SSR primarily arises from AVC integrators in high SCR conditions (e.g., SCR > 10), with a substantially lower risk of SSR under weak grid conditions.
4) CC presents negative damping to SSR, though it mitigates SR. P gain of AVC can alleviate SSR, though it exacerbates SR. There are thus trade-offs. The bandwidth of CC is often set high to limit overcurrent during faults. Hence, to reduce the risk of SSR, it is suggested to properly increase the P gain of AVC, specifically for the highest SCR condition in practice.

APPENDIX I

Consider a cubic equation

$$s^3+(n_1+m_2)\,s^2+(n_0+m_1)\,s+m_0=0 \tag{35}$$

When the following conditions hold, i.e.,

$$n_0\gg m_1,\, n_0\gg \varepsilon=(n_1-m_0/n_0+m_2)\,m_0/n_0 \tag{36}$$

The factorization of polynomial can be approximated to

$$\begin{aligned} &s^3+(n_1+m_2)\,s^2+(n_0+m_1)\,s+m_0\\ &\approx\left[s^2+(n_1-m_0/n_0+m_2)\,s+n_0\right](s+m_0/n_0)\\ &=s^3+(n_1+m_2)\,s^2+(n_0+\varepsilon)\,s+m_0 \end{aligned} \tag{37}$$

$n_0\approx n_0+m_1\approx n_0+\varepsilon$ is used with the condition (36). Note that the condition (36) can be easily met when

$$n_0\gg n_1,\, n_0\gg m_i,\, i=0,1,2 \tag{38}$$

Consequently, the solutions of (37) are given as

$$\begin{aligned} p_{1,2}&\approx\frac{-n_1+\frac{m_0}{n_0}-m_2}{2}\pm j\sqrt{n_0-\left(\frac{n_1-\frac{m_0}{n_0}+m_2}{2}\right)^2},\\ p_3&\approx -m_0/n_0. \end{aligned} \tag{39}$$

APPENDIX II

This section derives the model of GFM control with PSC and AVC. Substituting (11) and (18) into (8) gives

$$\Delta\mathbf{i}=-j\frac{\mathbf{i}_0s^2+\left(2\alpha_a\mathbf{i}_0-\boldsymbol{\beta}_a\right)s+\left(\alpha_a^2+\omega_1^2\right)\mathbf{i}_0+\boldsymbol{\eta}_a}{(s+\alpha_a)^2+\omega_1^2}\Delta\theta \tag{40}$$

where $\alpha_a=R/L_{eqa}$, $L_{eqa}=L+G_aL_g$, $\boldsymbol{\beta}_a=(V+G_a\mathbf{E}_0)/L_{eqa}$ and $\boldsymbol{\eta}_a=-(\alpha_a-j\omega_1)\boldsymbol{\beta}_a$. By substituting (11) and (40) into (10), the equivalent PSC plant is given as

$$\begin{aligned} \Delta P&=\kappa\frac{\tau_{2a}s^2+\tau_{1a}s+\tau_{0a}}{(s+\alpha_a)^2+\omega_1^2}\Delta\theta=G_{\theta Pa}(s)\,\Delta\theta,\\ \tau_{2a}&=L_g\mathrm{Im}\left\{\mathbf{i}_0\boldsymbol{\beta}_a^*\right\},\ \tau_{1a}=\mathrm{Im}\left\{\mathbf{E}_0\boldsymbol{\beta}_a^*\right\}-\omega_1L_g\mathrm{Re}\left\{\mathbf{i}_0\boldsymbol{\beta}_a^*\right\}\\ &\quad+L_g\mathrm{Im}\left\{\mathbf{i}_0^*\boldsymbol{\eta}_a\right\},\ \tau_{0a}=\mathrm{Im}\left\{\mathbf{E}_0^*\boldsymbol{\eta}_a\right\}+\omega_1L_g\mathrm{Re}\left\{\mathbf{i}_0\boldsymbol{\eta}_a^*\right\} \end{aligned} \tag{41}$$

Comparing with (12), the inclusion of AVC dynamics makes the equivalent PSC plant more complex. By substituting $G_{\theta P}(s)$ in Fig. 2 with $G_{\theta Pa}(s)$, the closed-loop transfer function of PSC is given as

$$\begin{aligned} \Delta P&=\frac{[k_P/(\kappa s)]\,G_{\theta Pa}(s)}{1+[k_P/(\kappa s)]\,G_{\theta Pa}(s)}\Delta P_{\mathrm{ref}}=G_{\mathrm{PSC}a}(s)\,\Delta P_{\mathrm{ref}},\\ G_{\mathrm{PSC}a}(s)&=\frac{k_P\left(\tau_{2a}s^2+\tau_{1a}s+\tau_{0a}\right)}{s^3+(2\alpha_a+k_P\tau_{2a})\,s^2+\left(\alpha_a^2+\omega_1^2+k_P\tau_{1a}\right)s+k_P\tau_{0a}} \end{aligned} \tag{42}$$

$G_{\mathrm{PSC}a}(s)$ has three poles. Define the coefficients $n_{1a}=2\alpha_a$, $n_{0a}=\omega_1^2$, $m_{2a}=k_P\tau_{2a}$, $m_{1a}=\alpha_a^2+k_P\tau_{1a}$ and $m_{0a}=k_P\tau_{0a}$, and substitute them into the denominator of $G_{\mathrm{PSC}a}(s)$. Then, the poles of $G_{\mathrm{PSC}a}(s)$ can be solved by setting the denominator equal to 0, i.e.,

$$s^3+(n_{1a}+m_{2a})\,s^2+(n_{0a}+m_{1a})\,s+m_{0a}=0 \tag{43}$$

Using the rules in Appendix I, the closed-form solutions of the three poles can be approximately derived as

$$\begin{aligned} G_{\mathrm{PSC}a}(s)&\approx\frac{k_P\left(\tau_{2a}s^2+\tau_{1a}s+\tau_{0a}\right)}{(s-p_{1a})\,(s-p_{2a})\,(s-p_{3a})}\Delta P_{\mathrm{ref}},\\ p_{1,2a}&=-\alpha_a+\frac{k_P\tau_{0a}}{2\omega_1^2}-\frac{k_P\tau_{2a}}{2}\pm j\sqrt{D}\\ p_{3a}&=-k_P\tau_{0a}/\omega_1^2\\ D&=\omega_1^2-\left(2\alpha_a-k_P\tau_{0a}/\omega_1^2+k_P\tau_{2a}\right)^2/4 \end{aligned} \tag{44}$$

Further, considering that $\alpha_a\ll\omega_1$ and $k_P\ll\omega_1$, the approximations $\boldsymbol{\eta}_a\approx j\omega_1\boldsymbol{\beta}_a$ and $D\approx\omega_1^2$ can be used. Then, with (41), the final closed-form solutions of the poles are given as

$$\begin{aligned} p_{1,2a}&\approx-\frac{R-\delta}{L+G_aL_g}\pm j\omega_1,\ \delta=k_P\left(VE_{d0}+G_a|\mathbf{E}_0|^2\right)/(2\omega_1)\\ p_{3a}&=-\frac{2\delta+k_PL_g\left(Vi_{q0}+G_a\mathrm{Im}\left\{\mathbf{E}_0^*\mathbf{i}_0\right\}\right)}{L+G_aL_g} \end{aligned} \tag{45}$$

Finally, substituting the coefficients into m_i and n_i ($i = 0, 1, 2$) in gives the solutions (15).

APPENDIX III

This section derives the model of GFM control with PSC, AVC (P controller), CC and VFF. Substituting (11) and (23) into (8) gives

$$\Delta \mathbf{i} = -j\frac{\mathbf{i}_0 s^2+\left(\alpha_b \mathbf{i}_0-\boldsymbol{\beta}_b\right) s+\left(\omega_1^2+j\omega_1\alpha_b\right)\mathbf{i}_0-\left(\alpha_b-j\omega_1\right)\boldsymbol{\beta}_b}{(s+\alpha_b)^2+\omega_1^2}\Delta\theta \tag{46}$$

where $\alpha_b = (R + R_a)/L_{eqb} \approx R_a/L_{eqb}$, $L_{eqb} = L + (R_aG_a - 1)L_g$ and $\boldsymbol{\beta}_b = [V + (R_aG_a - 1)\mathbf{E}_0]/L_{eqb}$.

Note that R_a acts as a virtual resistance in series with L, and it is much higher than the ESR R, thus R can be omitted. In contrast, the AVC controller gain G_a increases the equivalent inductance, as indicated by L_{eqb}, while the voltage feedforward has a counteractive effect (the term "-1" in L_{eqb}).

By substituting (11) and (46) into (10), the equivalent PSC plant, which includes the AVC and CC dynamics, is given as

$$\begin{aligned}
&\Delta P = \kappa\frac{\tau_{2b}s^2+\tau_{1b}s+\tau_{0b}}{(s+\alpha_b)^2+\omega_1^2}\Delta\theta = G_{\theta Pb}(s)\,\Delta\theta,\\
&\tau_{2b} = L_g\mathrm{Im}\left\{\mathbf{i}_0\boldsymbol{\beta}_b^*\right\}\\
&\tau_{1b} = -\alpha_b\mathrm{Im}\left\{\mathbf{E}_0^*\mathbf{i}_0\right\}+\mathrm{Im}\left\{\mathbf{E}_0\boldsymbol{\beta}_b^*\right\}-\omega_1L_g\mathrm{Re}\left\{\mathbf{i}_0\boldsymbol{\beta}_b^*\right\}\\
&\qquad +L_g\mathrm{Re}\left\{j\mathbf{i}_0\boldsymbol{\eta}_b^*\right\},\ \tau_{0b} = \omega_1\alpha_b\mathrm{Re}\left\{\mathbf{E}_0^*\mathbf{i}_0\right\}+\mathrm{Re}\left\{j\mathbf{E}_0\boldsymbol{\eta}_b^*\right\}\\
&\qquad +\omega_1L_g\mathrm{Im}\left\{j\mathbf{i}_0\boldsymbol{\eta}_b^*\right\}-\left(\mathrm{Im}\left\{\mathbf{E}_0^*\mathbf{i}_0\right\}+\omega_1L_g|\mathbf{i}_0|^2\right)\alpha_b^2
\end{aligned} \tag{47}$$

where $\boldsymbol{\eta}_b = -(\alpha_b - j\omega_1)\boldsymbol{\beta}_b$. By substituting $G_{\theta P}(s)$ in Fig. 2 with $G_{\theta Pb}(s)$, the closed-loop transfer function is given as

$$\begin{aligned}
\Delta P &= \frac{[k_P/(\kappa s)]\,G_{\theta Pb}(s)}{1+[k_P/(\kappa s)]\,G_{\theta Pb}(s)}\Delta P_{\mathrm{ref}} = G_{\mathrm{PSC}b}(s)\,\Delta P_{\mathrm{ref}}\\
&= \frac{k_P\left(\tau_{2b}s^2+\tau_{1b}s+\tau_{0b}\right)}{s^3+(2\alpha_b+k_P\tau_{2b})s^2+\left(\alpha_b^2+\omega_1^2+k_P\tau_{1b}\right)s+k_P\tau_{0b}}\Delta P_{\mathrm{ref}}.
\end{aligned} \tag{48}$$

$G_{\mathrm{PSC}b}(s)$ has three poles. Define the coefficients $n_{1b} = 2\alpha_b$, $n_{0b} = \alpha_b^2 + \omega_1^2$, $m_{2b} = k_P\tau_{2b}$, $m_{1b} = k_P\tau_{1b}$ and $m_{0b} = k_P\tau_{0b}$, and substitute them into the denominator of $G_{\mathrm{PSC}b}(s)$. Then, the poles of $G_{\mathrm{PSC}b}(s)$ can be solved by setting the denominator equal to 0, i.e.,

$$s^3 + (n_{1b} + m_{2b})s^2 + (n_{0b} + m_{1b})s + m_{0b} = 0 \tag{49}$$

Using the rules in Appendix I, the closed-form solutions of the three poles can be approximately derived as

$$\begin{aligned}
&G_{\mathrm{PSC}b}(s) \approx \frac{k_P\left(\tau_{2b}s^2+\tau_{1b}s+\tau_{0b}\right)}{(s-p_{1b})(s-p_{2b})(s-p_{3b})}\Delta P_{\mathrm{ref}},\\
&p_{1,2b} = -\alpha_b + \frac{k_P\tau_{0b}}{2\left(\alpha_b^2+\omega_1^2\right)} - \frac{k_P\tau_{2b}}{2} \pm j\sqrt{F},\\
&p_{3b} = -\frac{k_P\tau_{0b}}{\left(\alpha_b^2+\omega_1^2\right)},\ F = \alpha_b^2+\omega_1^2\\
&\qquad -\left[2\alpha_b - k_P\tau_{0b}/\left(\alpha_b^2+\omega_1^2\right)+k_P\tau_{2b}\right]^2/4.
\end{aligned} \tag{50}$$

Since CC gives a high value of virtual resistance R_a, the coefficient $\alpha_b \approx R_a/L_{eqb}$ is comparable to ω_1 and cannot be omitted. Then, considering $k_P \ll \omega_1$, one can simply finds that

$$\alpha_b \gg \frac{k_P\tau_{0b}}{2\left(\alpha_b^2+\omega_1^2\right)} - \frac{k_P\tau_{2b}}{2} \tag{51}$$

and $F \approx \omega_1$. As a result, the conjugate poles $p_{1,2b}$ can be further simplified to

$$p_{1,2b} \approx -\alpha_b \pm j\omega_1 = -\frac{R+R_a}{L+(R_aG_a-1)L_g} \pm j\omega_1 \tag{52}$$

(52) shows that $p_{1,2b}$ are very closed to the poles of equivalent PSC plant in (47).

APPENDIX IV

This section derives the model of GFM control with PSC, AVC (PI controller), CC and VFF. Substituting (11) and (28) into (8) gives

$$\Delta \mathbf{i} = -j\frac{\left[s+\alpha_{c0}+j\omega_1(1+\mu/s)\right]\mathbf{i}_0-\boldsymbol{\beta}_c(s)}{s+\alpha_c+j\omega_1(1+\mu/s)}\Delta\theta \tag{53}$$

where

$$\begin{aligned}
&L_{eqc} = L+(R_aG_a-1)L_g,\ \mu = R_ak_iL_g/L_{eqc},\\
&\alpha_{c0} = R/L_{eqc}+\mu,\ \alpha_c = (R+R_a)/L_{eqc}+\mu \approx R_a/L_{eqc}\\
&\qquad +\mu,\ \boldsymbol{\beta}_c(s) = [V+(R_aG_a-1)\mathbf{E}_0+R_ak_i\mathbf{E}_0/s]/L_{eqc}.
\end{aligned} \tag{54}$$

Considering the light-load conditions and substituting $\mathbf{i}_0 \approx 0$ into (53) gives

$$\Delta \mathbf{i} \approx j\frac{\boldsymbol{\beta}_c(s)}{s+\alpha_c+j\omega_1(1+\mu/s)}\Delta\theta \tag{55}$$

Then by omitting s in the denominator, i.e., the SR mode, (55) can be further simplified to

$$\Delta \mathbf{i} \approx j\frac{\boldsymbol{\beta}_c(s)}{\alpha_c+j\omega_1(1+\mu/s)}\Delta\theta. \tag{56}$$

This simplification has minor influence on the accuracy of the model when the frequency is lower than ω_1 (e.g., 0∼25 Hz), as the magnitude of s is normally much lower than $\omega_1\mu/s$ in (55). This allows us to focus on SSR in a lower-frequency range. In addition, with $\mathbf{i}_0 \approx 0$, the static PCC voltage vector becomes

$$\mathbf{E}_0 = V - \left[(s+j\omega_1)L_f+R\right]\mathbf{i}_0 \approx V. \tag{57}$$

By substituting (56), (57) and $\mathbf{i}_0 \approx 0$ into (10), the equivalent PSC plant is given as

$$\Delta P = G_{\theta Pc}(s)\,\Delta\theta \approx \kappa V\,\Delta i_d$$

$$= \kappa \frac{V}{\alpha_c^2+\omega_1^2} \frac{\gamma\omega_1 s^2 + (\tau+\mu\gamma)\omega_1 s + \omega_1\mu\tau}{s^2 + \frac{2\omega_1^2\mu}{\alpha_c^2+\omega_1^2} s + \frac{\omega_1^2\mu^2}{\alpha_c^2+\omega_1^2}} \Delta\theta \tag{58}$$

where $\gamma = R_a G_a V/L_{eqc}$ and $\tau = R_a k_i V/L_{eqc}$.

By substituting $G_{\theta P}(s)$ in Fig. 2 with $G_{\theta Pc}(s)$, the closed-loop transfer function is given as

$$\begin{aligned}\Delta P &= \frac{[k_P/(\kappa s)]\, G_{\theta Pc}(s)}{1+[k_P/(\kappa s)]\, G_{\theta Pc}(s)} \Delta P_{\text{ref}} = G_{\text{PSCc}}(s)\, \Delta P_{\text{ref}} \\ &= \frac{m_{2c}s^2 + n_{0c}s + m_{0c}}{s^3 + (n_{1c}+m_{2c})s^2 + (n_{0c}+m_{1c})s + m_{0c}} \Delta P_{\text{ref}}\end{aligned} \tag{59}$$

where

$$\begin{aligned} m_{2c} &= \frac{k_P V\gamma\omega_1}{\alpha_c^2+\omega_1^2}, m_{1c} = \frac{\omega_1^2\mu^2}{\alpha_c^2+\omega_1^2}, m_{0c} = \frac{k_P V\omega_1\mu\tau}{\alpha_c^2+\omega_1^2}, \\ n_{1c} &= \frac{2\omega_1^2\mu}{\alpha_c^2+\omega_1^2}, n_{0c} = \frac{k_P V(\tau+\mu\gamma)\omega_1}{\alpha_c^2+\omega_1^2}. \end{aligned} \tag{60}$$

Note that n_{0c} is defined as a coefficient in the nominator, which is different from the previous schemes. This is to meet the conditions in Appendix I.

Then, the poles of $G_{\text{PSCc}}(s)$ can be solved by setting the denominator equal to 0, i.e.,

$$s^3 + (n_{1c}+m_{2c})s^2 + (n_{0c}+m_{1c})s + m_{0c} = 0 \tag{61}$$

Using the rules in Appendix I with the coefficients in (54) and (60), the closed-form solutions of the three poles can be approximately derived as

$$\begin{aligned} G_{\text{PSCc}}(s) &\approx \frac{m_{2c}s^2 + n_{0c}s + m_{0c}}{(s-p_{1c})(s-p_{2c})(s-p_{3c})} \Delta P_{\text{ref}} \\ p_{1,2c} &= (\rho_1-\rho_2)\frac{R_a k_i L_g}{2L_{eqc}} - \frac{k_P G_a \psi}{2} \\ &\quad \pm j\sqrt{\frac{k_i k_P \psi}{\rho_1} - \left[(\rho_1-\rho_2)\frac{R_a k_i L_g}{2L_{eqc}} - \frac{k_P G_a \psi}{2}\right]^2}, \\ p_{3c} &= -\frac{R_a k_i L_g}{L_f + 2R_a L_g G_a} \end{aligned} \tag{62}$$

where

$$\begin{aligned} \rho_1 &= \frac{L_f + R_a L_g G_a}{L_f + 2R_a L_g G_a}, \rho_2 = \frac{2}{\left[\frac{R_a(1+k_i L_g)}{\omega_1 L_{eqc}}\right]^2 + 1}, \\ \psi &= \frac{V^2 R_a/\omega_1 L_{eqc}}{\left[\frac{R_a(1+k_i L_g)}{\omega_1 L_{eqc}}\right]^2 + 1} \end{aligned} \tag{63}$$

APPENDIX V

It is apparent that the imaginary part of $p_{1,2c}$ in (62) satisfies

$$\sqrt{\frac{k_i k_P \psi}{\rho_1} - \left[(\rho_1-\rho_2)\frac{R_a k_i L_g}{2L_{eqc}} - \frac{k_P G_a \psi}{2}\right]^2} < \sqrt{\frac{k_i k_P \psi}{\rho_1}} \tag{64}$$

When the grid is stiff, i.e., $L_g \approx 0$, the coefficient ρ_1 in (63) can be approximated to 1. Then substitute ψ in (63) and $\rho_1 \approx 1$ into (64) gives

$$\sqrt{\frac{k_i k_P \psi}{\rho_1}} \approx \sqrt{k_i k_P \frac{V^2 R_a \omega_1 L_{eqc}}{R_a^2(1+k_i L_g)^2 + \omega_1^2 L_{eqc}^2}} \tag{65}$$

For a typical design of CC gain $R_a \approx 1$ (to give a bandwidth around 500 Hz [23]), it is simple to find $R_a(1+k_i L_g) > \omega_1 L_{eqc}$. Hence, (65) has

$$\begin{aligned} &\sqrt{k_i k_P \frac{V^2 R_a \omega_1 L_{eqc}}{R_a^2(1+k_i L_g)^2 + \omega_1^2 L_{eqc}^2}} < \sqrt{k_i k_P \frac{V^2 R_a \omega_1 L_{eqc}}{2\omega_1^2 L_{eqc}^2}} \\ &= \sqrt{k_i k_P \frac{V^2 R_a}{2\omega_1 L_{eqc}}} < \sqrt{k_i k_P \frac{V^2 R_a}{2\omega_1 L_f}} \end{aligned} \tag{66}$$

In addition, the droop value is often low, e.g., $k_P \leqslant 0.05\omega_1$. The L-filter of converter is often around 0.1 p.u., thus R_a/L_f is close to $10\omega_1$. Then, with these conditions, (66) finally has

$$\sqrt{k_i k_P \frac{V^2 R_a}{2\omega_1 L_f}} \leqslant \sqrt{0.25 k_i \omega_1 V^2} \tag{67}$$

APPENDIX VI

Substituting L_{eqc} in (54) and (63) into $\rho_2 > 1$ gives

$$\begin{aligned} \rho_2 > 1 &\Rightarrow \frac{R_a(1+k_i L_g)}{\omega_1(L_f + R_a G_a L_g)} < 1 \\ &\Rightarrow (G_a - k_i/\omega_1)\omega_1 L_g > 1 - \omega_1 L_f/R_a. \end{aligned} \tag{68}$$

If the parameters are designed to meet $G_a - k_i/\omega_1 > 0$, then (68) has

$$\omega_1 L_g > \frac{1-\omega_1 L_f/R_a}{G_a - k_i/\omega_1}. \tag{69}$$

With SCR calculated in (1), we can find

$$\text{SCR} < \frac{G_a - k_i/\omega_1}{1-\omega_1 L_f/R_a}. \tag{70}$$

REFERENCES

[1] R. H. Lasseter, Z. Chen, and D. Pattabiraman, "Grid-forming inverters: A critical asset for the power grid," *IEEE J. Emerg. Sel. Topics Power Electron.*, vol. 8, no. 2, pp. 925–935, Jun. 2020.

[2] North American Electric Reliability Corporation (NERC), "Grid forming technology," *White Paper*, Dec. 2021. [Online]. Available: https://www.nerc.com/

[3] B. Kroposki et al., "UNIFI specifications for grid-forming inverter-based resources—Version 1," Tech. Rep. UNIFI-2022-2-1, Dec. 2022.

[4] A. Johnson, "Minimum specification required for provision of GB grid forming (GBGF) capability (formerly virtual synchronous machine/VSM capability)," Nat. Grid ESO, Warwick, U.K., Tech. Rep. GC 0137, Nov. 2021. [Online]. Available: https://www.nationalgrideso.com/

[5] Y. Lin et al., "Research roadmap on grid-forming inverters," National Renewable Energy Laboratory, Golden, CO, Tech. Rep. NREL/TP-5D00-73476, 2020. [Online]. Available: https://www.nrel.gov/docs/fy21osti/73476.pdf

[6] L. Zhang, L. Harnefors, and H.-P. Nee, "Power-synchronization control of grid-connected voltage-source converters," *IEEE Trans. Power Syst.*, vol. 25, no. 2, pp. 809–820, May 2010.
[7] Q. Taoufik, "Grid-forming control to achieve a 100% power electronics interfaced power transmission systems," in *Electric Power*. Paris, France: HESAM Université, 2020.
[8] L. Harnefors, M. Hinkkanen, U. Riaz, F. M. M. Rahman, and L. Zhang, "Robust analytic design of power-synchronization control," *IEEE Trans. Ind. Electron.*, vol. 66, no. 8, pp. 5810–5819, Aug. 2019.
[9] F. Zhao, X. Wang, Z. Zhou, Y. Sun, L. Harnefors, and T. Zhu, "Robust grid-forming control with active susceptance," *IEEE Trans. Power Electron.*, vol. 38, no. 3, pp. 2872–2877, Mar. 2023.
[10] L. Harnefors, J. Kukkola, M. Routimo, M. Hinkkanen, and X. Wang, "A universal controller for grid-connected voltage-source converters," *IEEE J. Emerg. Sel. Topics Power Electron.*, vol. 9, no. 5, pp. 5761–5770, Oct. 2021.
[11] F. Zhao, X. Wang, and T. Zhu, "Power dynamic decoupling control of grid-forming converter in stiff grid," *IEEE Trans. Power Electron.*, vol. 37, no. 8, pp. 9073–9088, Aug. 2022.
[12] Y. Li, Y. Gu, and T. C. Green, "Revisiting grid-forming and grid-following inverters: A duality theory," *IEEE Trans. Power Syst.*, vol. 37, no. 6, pp. 4541–4554, Nov. 2022.
[13] Y. Liao, X. Wang, F. Liu, K. Xin, and Y. Liu, "Sub-synchronous control interaction in grid-forming VSCs with droop control," in *Proc. 4th IEEE Workshop Electron. Grid*, 2019, pp. 1–6.
[14] G. Li et al., "Analysis and mitigation of subsynchronous resonance in series-compensated grid-connected system controlled by a virtual synchronous generator," *IEEE Trans. Power Electron.*, vol. 35, no. 10, pp. 11096–11107, Oct. 2020.
[15] G. Denis, "From grid-following to grid-forming: The new strategy to build 100% power-electronics interfaced transmission system with enhanced transient behavior," Ph.D. Thesis, Ecole Centrale de Lille, Nov. 2017.
[16] R. Rosso, X. Wang, M. Liserre, X. Lu, and S. Engelken, "Grid-forming converters: Control approaches, grid-synchronization, and future trends—A review," *IEEE Open J. Ind. Appl.*, vol. 2, pp. 93–109, 2021.
[17] L. Zhang, "Modeling and control of VSC-HVDC links connected to weak AC systems," Ph.D. dissertation, Dept. School Elect. Eng., Stockholm, Sweden, 2011.
[18] L. Harnefors, "Modeling of three-phase dynamic systems using complex transfer functions and transfer matrices," *IEEE Trans. Ind. Electron.*, vol. 54, no. 4, pp. 2239–2248, Aug. 2007.
[19] U. Markovic, O. Stanojev, P. Aristidou, E. Vrettos, D. Callaway, and G. Hug, "Understanding small-signal stability of low-inertia systems," *IEEE Trans. Power Syst.*, vol. 36, no. 5, pp. 3997–4017, Sep. 2021.
[20] W. Du et al., "A comparative study of two widely used grid-forming droop controls on microgrid small-signal stability," *IEEE J. Emerg. Sel. Topics Power Electron.*, vol. 8, no. 2, pp. 963–975, Jun. 2020.
[21] E. Rokrok, T. Qoria, A. Bruyere, B. Francois, and X. Guillaud, "Transient stability assessment and enhancement of grid-forming converters embedding current reference saturation as current limiting strategy," *IEEE Trans. Power Syst.*, vol. 37, no. 2, pp. 1519–1531, Mar. 2022.
[22] B. Fan, T. Liu, F. Zhao, H. Wu, and X. Wang, "A review of current-limiting control of grid-forming inverters under symmetrical disturbances," *IEEE Open J. Power Electron.*, vol. 3, pp. 955–969, 2022.
[23] L. Harnefors, M. Bongiorno, and S. Lundberg, "Input-admittance calculation and shaping for controlled voltage-source converters," *IEEE Trans. Ind. Electron.*, vol. 54, no. 6, pp. 3323–3334, Dec. 2007.
[24] D. G. Holmes, T. A. Lipo, B. P. McGrath, and W. Y. Kong, "Optimized design of stationary frame three phase AC current regulators," *IEEE Trans. Power Electron.*, vol. 24, no. 11, pp. 2417–2426, Nov. 2009.
[25] F. Zhao, X. Wang, Z. Zhou, Ł. Kocewiak, and J. R. Svensson, "Comparative study of battery-based STATCOM in grid-following and grid-forming modes for stabilization of offshore wind power plant," *Electric Power Syst. Res.*, vol. 212, Nov. 2022, Art. no. 108449.
[26] P. Rodriguez, I. Candela, C. Citro, J. Rocabert, and A. Luna, "Control of grid-connected power converters based on a virtual admittance control loop," in *Proc. 15th Eur. Conf. Power Electron. Appl.*, 2013, pp. 1–10.
[27] M. Schweizer, S. Almer, S. Pettersson, A. Merkert, V. Bergemann, and L. Harnefors, "Grid-forming vector current control," *IEEE Trans. Power Electron.*, vol. 37, no. 11, pp. 13091–13106, Nov. 2022.
[28] Y. Yu, M. Zhang, M. Antoine, and H. Li, "Analysis of synchronous frequency resonance in VSG based on the sequence impedance models," in *Proc. 22nd Int. Conf. Elect. Machines Syst.*, 2019, pp. 1–6.
[29] L. Harnefors and H. - P. Nee, "Model-based current control of AC machines using the internal model control method," *IEEE Open J. Ind. Appl.*, vol. 34, no. 1, pp. 133–141, Feb. 1998.

FANGZHOU ZHAO (Member, IEEE) received the B.S. degree in electrical engineering and automation from the University of Electronic Science and Technology of China, Chengdu, China, in 2014, and the Ph.D. degree in electrical engineering from Xi'an Jiaotong University, Xi'an, China, in 2019. He is currently an Assistant Professor with AAU Energy, Aalborg University, Aalborg, Denmark, where he was a Postdoctoral Researcher from 2020 to 2022. His research interests include modeling and stability analysis of power electronics-based power systems, grid-forming control design, and grid emulation system.

TIANHUA ZHU (Member, IEEE) received the B.S., M.S., and Ph. D. degrees in electrical engineering from Xi'an Jiaotong University, Xi'an, China, in 2014, 2017, and 2020, respectively. Since 2020, she has been with the Department of Energy, Aalborg University, Aalborg, Denmark, where she is currently a Postdoctoral Researcher. Her research interests include modeling and control of power factor correction converters, resonant converters, characteristics and application of GaN devices, maximum power point tracking techniques, and distributed maximum power point tracking.

LENNART HARNEFORS (Fellow, IEEE) received the M.Sc., Licentiate, and Ph.D. degrees in electrical engineering from the Royal Institute of Technology (KTH), Stockholm, Sweden, and the Docent (D.Sc.) degree in industrial automation from Lund University, Lund, Sweden, in 1993, 1995, 1997, and 2000, respectively. During 1994–2005, he was with Mälardalen University, Västerås, Sweden and a Professor of electrical engineering from 2001. Duing 2001–2005, he was a part-time Visiting Professor of electrical drives with the Chalmers University of Technology, Göteborg, Sweden. In 2005, he joined ABB, HVDC Product Group, Ludvika, Sweden, where he, among other responsibilities, led the control development for the first generation of multilevel-converter HVDC Light. In 2012, he joined ABB, Corporate Research, Västerås, where he was appointed as a Senior Principal Scientist in 2013 and a Corporate Research Fellow in 2021. He was a part-time Adjunct Professor of power electronics with KTH during 2011–2023. He is currently a part-time Visiting Professor with Aalto University, Helsinki, Finland. His research interests include control and dynamic analysis of power electronic systems, particularly grid-connected converters, and AC drives. He is the Editor of IEEE JOURNAL OF EMERGING AND SELECTED TOPICS IN POWER ELECTRONICS.

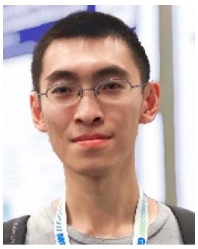

BO FAN (Member, IEEE) received the B.S. degree in automation, and the Ph.D. degree in control science and engineering from Zhejiang University, Hangzhou, China, in 2014 and 2019, respectively.

From 2018 to 2019, he was a Visiting Predoctoral Fellow with Lehigh University, Bethlehem, PA, USA. From 2020 to 2023, he was a Postdoctoral Researcher with Aalborg University, Aalborg, Denmark. Since 2023, he has been a Visiting Postdoctoral Researcher with the KTH Royal Institute of Technology, Stockholm, Sweden. His research interests include power system stability, power electronics, smart grid, distributed control, and nonlinear systems.

He was the recipient of the Best Reviewer Award of IEEE TRANSACTIONS ON SMART GRID in 2019, Outstanding Reviewer Awards of IEEE TRANSACTIONS ON POWER SYSTEMS in 2019 and 2021, Chinese Association of Automation Excellent Doctoral Dissertation Award in 2020, and Marie Skłodowska-Curie Individual Fellowship in 2021.

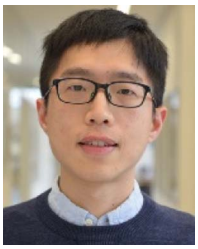

HENG WU (Member, IEEE) received the B.S. and M.S. degrees in electrical engineering from the Nanjing University of Aeronautics and Astronautics, Nanjing, China, in 2012 and 2015, respectively, and the Ph.D. degree in electrical engineering from Aalborg University, Aalborg, Denmark, in 2020. He is currently an Assistant Professor and a Leader of Electronic Power Grid (eGRID) Research Group with AAU Energy, Aalborg University. From 2015 to 2017, he was an Electrical Engineer with NR Electric Company Ltd, Nanjing. He was a guest researcher with Ørsted Wind Power, Fredericia, Denmark, in 2018, and Bundeswehr University Munich, Munich, Germany, in 2019. From 2020 to 2021, he was a Postdoctoral Researcher with Aalborg University. He is the Chairman of IEEE Task Force on Frequency-domain Modeling and Dynamic Analysis of HVDC and FACTS, the subgroup leader of Cigre working group B4/C4.93, a Member of GB grid forming best practice expert group formed by national grid ESO, U.K. and Technical Committee, European Academy of Wind Energy. His research interests include the modelling and stability analysis of the power electronic based power systems. From 2019, he is identified as world's top 2% scientist by Stanford University, Stanford, CA, USA. He was the recipient of the 2019 Outstanding Reviewer Award of IEEE TRANSACTIONS ON POWER ELECTRONICS and 2021 Star Reviewer Award of the IEEE JOURNAL OF EMERGING AND SELECTED TOPICS IN POWER ELECTRONICS.

ZICHAO ZHOU (Student Member, IEEE) received the B.S. degree in electrical engineering and automation and the M.S. degree in electrical engineering from the Harbin Institute of Technology, Harbin, China, in 2017 and 2019, respectively. He is currently working toward the Ph.D. degree in power electronic engineering with the KTH Royal Institute of Technology, Stockholm, Sweden. His research interests include modeling and stability analysis of power electronics systems.

YIN SUN (Member, IEEE) received the B.Sc. degree in electrical engineering from the Harbin Institute of Technology, Harbin, China, in 2008, the M.Sc. degree in sustainable energy technology from Twente University, Enschede, The Netherlands, in 2010, and the Ph.D. degree in stability and control of the power electronics dominant grid from the Eindhoven University of Technology, Eindhoven, The Netherlands, in 2018. He is a Senior Electrical Engineer at Shell, Subject Matter Expert of power system analysis, HVDC and power converters with Instrument Control and Electrical (ICE) Discipline, Shell Projects & Technology. He is also a part-time Associated Professor focusing on grid connection technology with the Electrical Energy System Group, Eindhoven University of Technology (TU/e).

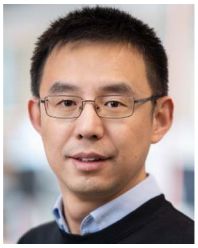

XIONGFEI WANG (Fellow, IEEE) received the B.S. degree in electrical engineering from Yanshan University, Qinhuangdao, China, in 2006, the M.S. degree in electrical engineering from the Harbin Institute of Technology, Harbin, China, in 2008, and the Ph.D. degree in energy technology from Aalborg University, Aalborg, Denmark, in 2013.

From 2009 to 2022, he was with Aalborg University where he became an Assistant Professor in 2014, an Associate Professor in 2016, a Professor and Leader of Electronic Power Grid (eGRID) Research Group in 2018. From 2022, was a Professor with the KTH Royal Institute of Technology, Stockholm, Sweden, and a part-time Professor with Aalborg University. His research interests include modeling and control of power electronic converters and systems, stability and power quality of power-electronic-dominated power systems, and high-power converters.

He is an Executive Editor (Editor-in-Chief) of IEEE TRANSACTIONS ON POWER ELECTRONICS LETTERS and an Associate Editor for IEEE JOURNAL OF EMERGING AND SELECTED TOPICS IN POWER ELECTRONICS. was the recipient of the 10 IEEE Prize Paper Awards, 2016 AAU Talent for Future Research Leaders, 2018 Richard M. Bass Outstanding Young Power Electronics Engineer Award, 2019 IEEE PELS Sustainable Energy Systems Technical Achievement Award, and 2022 Isao Takahashi Power Electronics Award.